Pre-Lithiated Li$_2$V$_6$O$_{13}$ Cathode Enables High-Energy Aluminum-Ion Battery

Shunlong Ju, Jikai Ye, Yang Meng, Guanglin Xia, and Xuebin Yu*

Owing to the low-cost, safety, and three-electron redox properties of aluminum, rechargeable aluminum-ion batteries (AIBs) are emerging as a promising energy storage technology. However, exploring suitable cathode material with both elevated working voltage and high reversible capacity remains a daunting challenge. Herein, under the guidance of density functional theory calculations, V$_6$O$_{13}$ is proposed as a promising cathode candidate in AIBs for the first time. It is demonstrated that aluminum ions are reversibly stored in V$_6$O$_{13}$ by intercalation reactions, with a high discharge voltage plateau of ≈1.1 V. Of particular note a pre-lithiation strategy is employed to further promote the redox kinetics, which endows the pre-lithiated V$_6$O$_{13}$ nanobelt (Li–VONB) with improved capacity of 161.6 mAh g^{-1} and impressive energy density of 177.7 Wh kg^{-1} after 300 cycles, far higher than other reported oxide cathodes in AIBs. Moreover, the shielding effect of pre-inserted Li and accelerated diffusion rate are uncovered at the atomic scale. This work develops a novel Li–VONB cathode for high-energy AIBs, and shows the great potential of pre-intercalation strategies in the application of AIBs.

1. Introduction

Because of the crustal abundance of aluminum resources, high theoretical capacity of three-electron redox properties, and the reliable safety, rechargeable AIBs are regarded as promising energy storage devices.[1,2] As with other secondary batteries, the energy density, which is determined collectively by the specific capacity and working voltage, is an important determinant for the commercial application of AIBs. Considering that metallic aluminum and ionic liquid are commonly used as anode and electrolyte, cathode material is believed to be the key to achieve high power and energy densities for AIBs.[3] In the past few years, numerous carbonaceous materials, conducting polymers, and metal compounds have been explored as cathodes in AIBs.[4–7] Among them, transition metal compounds (TMCs) have drawn great attention because of their high specific capacities.[8,9] Nevertheless, few studies focused on the

development and manipulation of TMC cathodes with elevated plateau voltages to boost the energy densities of AIBs. More efforts should be devoted into this topic to explore novel cathodes with advantages in both specific capacity and operation voltage.

The discharge voltage of intercalation type TMCs is determined by the crystal and electronic structure, elemental composition, and micro-morphology. As discussed in the previous literatures, the ionic character of the chemical bonds between transition metal cations and anions was proposed as an indicator to evaluate the electrochemical potential of cathode.[10] Following this rule, transition metal oxide, in which the highly electronegative oxygen anion would enable the chemical bonds to be more ionic, was predicted to achieve increased plateau voltage.[11] Particularly, vanadium-based oxides have shown the potentiality as high-voltage cathode materials as reported by recent studies, for which porous V$_2$O$_5$ could deliver a relatively high working voltage of ≈0.79 V, and molybdenum–vanadium oxide exhibited a discharge plateau at ≈0.75 V.[12,13] More importantly, the tunable chemical valences of vanadium elements and facile distortion of V–O bonds in vanadium-based oxides provide the possibility to screen more suitable candidates with higher operating voltage by optimizing their crystal structures and electron distributions.

Although the reported vanadium-based oxides demonstrated elevated working voltage, their reversible capacities and energy densities were unsatisfied, originating from the strong electrostatic interaction between the inserted Al^{3+} and the crystal lattice, which hindered the ionic intercalation and diffusion.[14] Pre-intercalation, as an effective approach, has been successfully employed in various battery systems, especially multivalent-ion batteries, to improve the electrochemical performance of intercalation type electrode materials.[15] The guest ions could expand the interlayer space and shield the electrostatic interaction between charge carriers and the lattice, leading to an accelerated diffusion kinetics.[16,17] Besides, the pre-intercalated ions and molecules could exist as "pillar" to stabilize the framework as well as to reduce the loss of crystallinity, increasing the structural stability of active materials during cycling.[18,19] Nevertheless, the pre-intercalation strategy has not been studied in AIBs so far. It is highly desirable to acquire high-performance vanadium-based oxides for AIBs applications by the attractive pre-intercalation method.

S. Ju, J. Ye, Y. Meng, G. Xia, X. Yu
Department of Materials Science
Fudan University
Shanghai 200433, China
E-mail: yuxuebin@fudan.edu.cn

Herein, pre-lithiation strategy was employed to optimize V_6O_{13} cathode, which was screened out from several vanadium oxides by its high theoretical voltage as predicted by density functional theory (DFT) calculations. The discharge voltage plateau of V_6O_{13} cathode was determined as ≈1.1 V and the Al^{3+} intercalation mechanism was confirmed. The produced Li–VONB delivered a reversible specific capacity of 161.6 mAh g^{-1} and remarkable energy density of 177.7 Wh kg^{-1} after 300 cycles. Moreover, DFT calculations elucidated that the pre-intercalated Li lowers the energy barriers of Al^{3+} migration by shielding electrostatic interactions and activating charge carriers. This work developed novel V_6O_{13} and $Li_2V_6O_{13}$ as promising cathodes for high-energy AIBs, and illustrated the superiority of pre-intercalation strategy for electrode design for advanced multivalent-ion batteries.

2. Results and Discussion

In order to accelerate the search for potential high-voltage cathode materials, DFT calculations were carried out to evaluate the theoretical working voltages of 12 common vanadium oxides, including V_2O_3 (space group: $R\bar{3}c$), VO_2 (space group: $C2/m$), VO_2 (space group: $P42/mnm$), V_2O_5 (space group: $Pmnm$), V_6O_{13} (space group: $C2/m$), and so on. The computational details are provided in Experimental Section. Although there is deviation between the simulated result and the actual discharge voltage, the calculations could reflect the voltage trends and are credible enough to be used for preliminary screening.[20,21] The optimized intercalation structures are listed in Figure S1, Supporting Information, and the corresponding theoretical voltages are summarized in **Figure 1**a. Among these vanadium oxides, V_6O_{13} exhibits significantly improved theoretical voltage for AIBs applications (1.97 V), making it a promising candidate for high-voltage cathode. Besides, it is well known that most transition metal oxides are semiconductors. V_2O_5, VO_2, V_5O_9, V_6O_{11}, and V_6O_{13} were exemplified to explore their electronic structures by projected density of state (PDOS) plots. As shown in Figure S2, Supporting Information, V_2O_5, VO_2, V_4O_7, and V_6O_{11} are semiconductors with band gaps of 2.29, 0.65, 0.58, and 0.78 eV, respectively. In contrast, metallic electronic structure is observed for V_6O_{13} by the density of state at the Fermi level in Figure 1b, which contributes to the enhanced conductivity. In summary, the predicted high working voltage and superior conductivity enable V_6O_{13} a promising cathode for AIBs.

Under the guidance of theoretical results, V_6O_{13} nanobelt (VONB) was prepared as cathode for nonaqueous AIBs by a two-step procedure as illustrated in **Figure 2**a. Aqueous solution composed of ammonium metavanadate and oxalic acid dihydrate was transferred into autoclave and heated at 180 °C to produce $NH_4V_4O_{10}$ (Figure S3, Supporting Information). Then it was calcinated at 450 °C and the final VONB was obtained. XRD pattern of the as-synthesized VONB is depicted in Figure 2b. The diffraction peaks are well indexed to V_6O_{13} phase (JCPDS No. 89–0100) and no other phases are detected, indicating the high purity of the final products. The crystal structure of V_6O_{13} is monoclinic (space group of $C2/m$) with alternating single and double VO_x layers, where the 3D interconnected lattice framework provides sufficient interstitial sites and tunnels for ion intercalation and migration. The morphology of VONB was subsequently investigated by scanning electron microscopy (SEM) and transmission electron microscopy (TEM). Figure 2c,d demonstrates the belt-like morphology of VONB with the length of hundreds of nanometers. The high-resolution TEM (HRTEM) images in Figure 2e clearly show an interplanar spacing of 0.58 nm, which is attributed to V_6O_{13} (200) plane. The lattice stripe of V_6O_{13} phase agrees well with the XRD result, further confirming the successful preparation of VONB sample. The nanobelt morphology of VONB is further confirmed by high-angle annular dark-field scanning TEM (HAADF-STEM) image, and the corresponding elemental mapping of energy-dispersive X-ray spectra (EDS) suggests the uniform distribution of V and O elements in VONB sample (Figure 2f).

The electrochemical behavior of VONB cathode was investigated in nonaqueous AIBs. As demonstrated in the galvanostatic charge/discharge profile in **Figure 3**a, there is a discharge plateau at ≈1.1 V and a charge plateau at ≈1.3 V for the VONB cathode under a current density of 50 mA g^{-1}, which correlates with the Al^{3+} uptake and removal, respectively. Clearly, the discharge plateau voltage is much higher than that of reported vanadium oxides,[22,23] confirming the high voltage feature of VONB predicted by DFT calculations. Although the initial discharge capacity of VONB is 173.6 mAh g^{-1}, it decays dramatically in a few cycles and the capacity retention is only 45.4 mAh g^{-1} after 50 cycles. To unravel the origin of the capacity fading, the Al^{3+} storage mechanism of V_6O_{13} was further studied. Ex situ XRD and XPS measurements were performed to identify the structural evolutions of VONB cathode during charging–discharging process. Figure 3b shows the XRD patterns of VONB cathode at different stages. In the entire
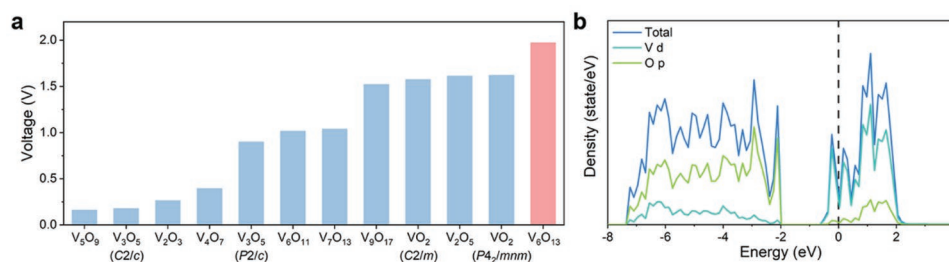

Figure 1. a) Predicted intercalation voltage of various vanadium oxides. b) PDOS of V_6O_{13}. The dashed line shows the Fermi level.
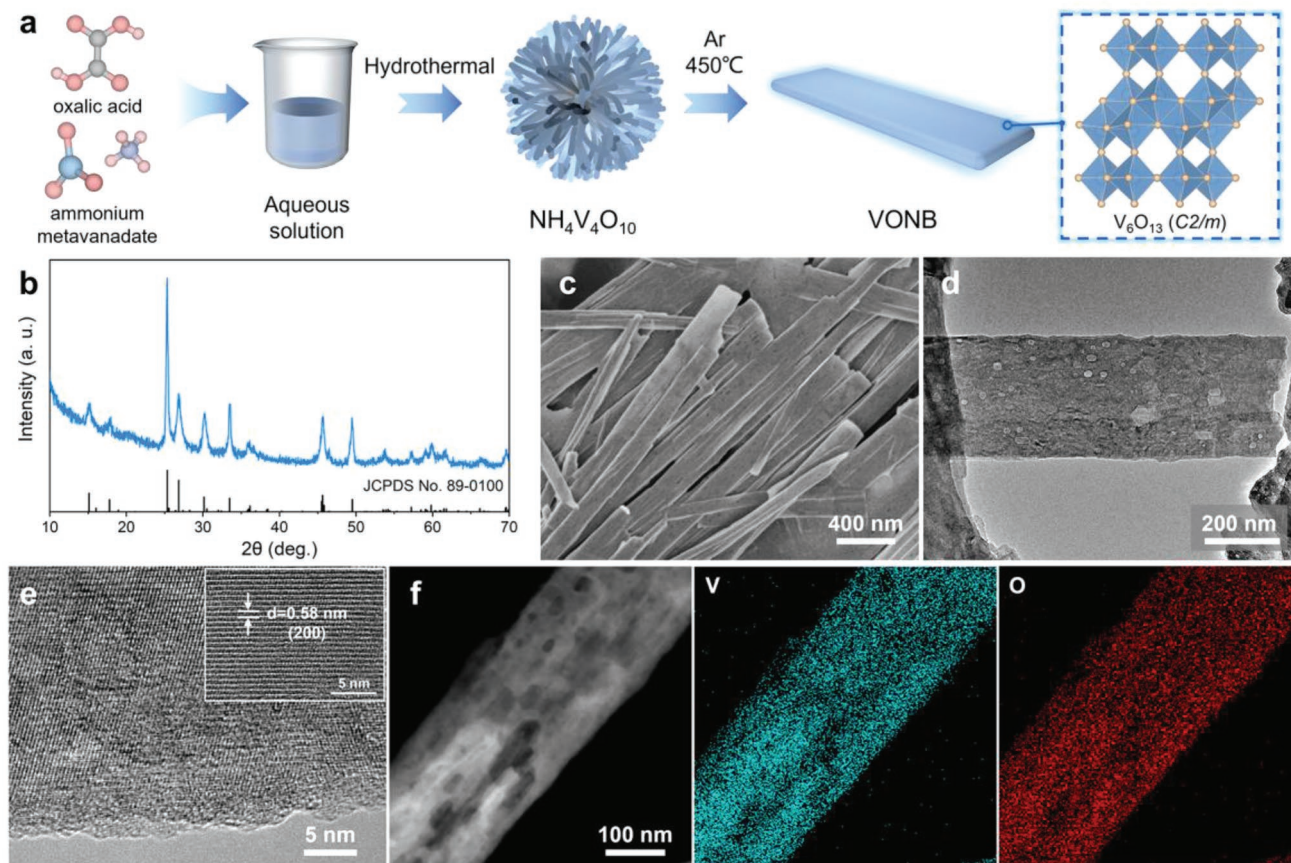
Figure 2. a) Schematic illustration of the synthesis of VONB. b) XRD patterns of VONB. c) SEM, d) TEM, and e) HRTEM images of VONB. f) HADDF-STEM image and EDS mapping images of elemental V and O in VONB.

electrochemical process, no peaks newly emerge or disappear in the XRD patterns, indicating the phase stability of V_6O_{13}. In the magnified XRD in Figure 3c, it is obvious that peak at ≈25°, which is indexed to the diffraction of V_6O_{13} (110) plane, shifts toward smaller angle at fully discharged stage and move back to higher angle at the end of charging process. The reversible variations of the (110) peak suggest the reversible change of lattice parameter. This phenomenon might be attributed to the intercalation of Al^{3+} into VONB during discharging process and the de-intercalation of Al^{3+} during charging process. However, the (110) peak could not recover to its initial position, implying that the intercalation/de-intercalation reactions are not completely reversible and some Al^{3+} are trapped in VONB. The unsatisfactory reversibility has a detrimental effect on the electrochemical performance and might be responsible for the capacity fading.

Furthermore, XPS analysis was applied to explore the valence changes of VONB during battery operation. From Al 2p spectra in Figure S4, Supporting Information, intensive Al 2p peak arisen at 75.4 eV is observed after discharging, and this peak becomes much weaker in the charging process, which confirms the intercalation/de-intercalation of Al^{3+} in VONB. Figure 3d illustrates the XPS spectra of V 2p of VONB collected at pristine, discharged, and charged states. Before cycling, characteristic of V^{5+} (peaks at 517.7 and 525.5 eV) and V^{4+} (peaks at 516.2 and 523.8 eV) are observed, indicating a multivalent

nature of VONB, which is consistent with previous studies.[24] When completely discharged, the intensity of V^{5+} valence state decreases along with the increased proportion of V^{4+}, and meanwhile a new valence state of V^{3+} appears (peaks at 515.3 and 523.0 eV). The conversion of the valence state is attributed to the Al^{3+} intercalation and the corresponding redox reactions. During the charging process, V^{3+} and V^{4+} are oxidized back to higher valence states because of the extraction of Al^{3+}. All these XPS results corroborate the reversible intercalation/de-intercalation of Al^{3+} in VONB in the electrochemical cycling. Besides, there are still some peaks for aluminum and low-valence vanadium after charging process, implying that a certain amount of Al^{3+} remains in the lattice of VONB and the redox reaction is not completely reversible, which is in accordance with the XRD results. In atomic scale, the intercalation of Al in VONB was simulated by DFT calculations. Al would locate at the interstitial site coordinating with the five neighboring O, and the intercalation formation energy (E_f) is −5.92 eV. This theoretical result suggests that the intercalation process is favorable thermodynamically (Figure S5, Supporting Information). The TEM and HRTEM images of VONB after discharging process are provided in Figure 3e,f. The discharged VONB exhibits belt-like morphology and the same lattice fringe as the pristine VONB, which might be ascribed to the sufficient interstitial space to accommodate Al without detectable lattice expansion,
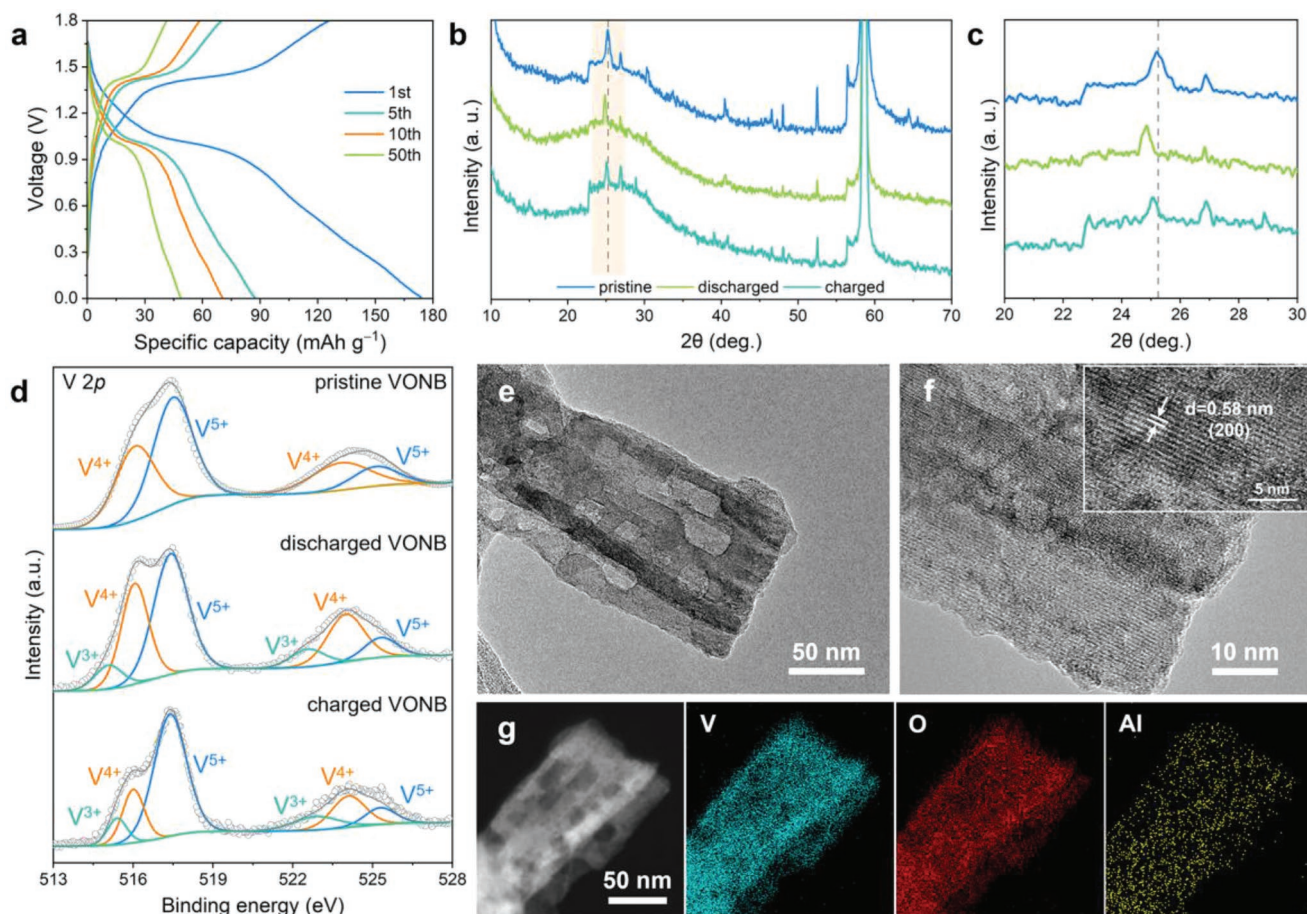
ADVANCED
SCIENCE NEWS
www.advancedsciencenews.com

ADVANCED
ENERGY
MATERIALS
www.advenergymat.de

Figure 3. a) Galvanostatic charge/discharge profiles of VONB cathode under 50 mA g^{-1}. b) Ex situ XRD patterns of VONB and c) the corresponding magnified image during the first charging–discharging process. d) Ex situ XPS spectra of V 2p for VONB at different stages. e) TEM and f) HRTEM images of VONB after first discharging. g) HADDF-STEM image and EDS mapping images of elemental V, O, and Al in discharged VONB.

indicating the structural stability of VONB. Moreover, the corresponding EDS mapping results in Figure 3g demonstrate the presence and uniform distribution of Al over VONB sample. All these results confirm the electrochemical intercalation/de-intercalation mechanism of Al^{3+} in VONB cathode during cycling.

Based on the discussions above, what hinders the application of VONB is the undesirable reversibility. Accordingly, pre-lithiation strategy was employed to promote the intercalation/de-intercalation process and accelerate the migration kinetics of Al^{3+} in V$_6$O$_{13}$ to improve the electrochemical properties. Li–VONB was synthesized by a facile hydrothermal method as shown in **Figure 4**a. VONB and lithium chloride were dissolved into aqueous solution and then treated at 180 °C. After centrifugation and washing, the final Li–VONB was obtained. The introduction of pre-inserted Li was proposed to shield the electrostatic interaction between cationic Al and anionic O, thus accelerating the migration of charge carriers. The XRD pattern of Li–VONB in Figure 4b could be indexed to the Li$_2$V$_6$O$_{13}$ phase (JCPDS No. 87–0471), indicating that Li–VONB delivers the same monoclinic crystal structure with $C2/m$ space group as VONB. The major difference is that there are new diffraction peaks at 24.8°, 31.2°, 33.3°, 42.1°, and 46.7° for Li–VONB,

which are originated from the pre-intercalated Li (Figure 4c). The detailed composition and valence state of Li–VONB were investigated through XPS measurement. High resolution Li 1s spectra demonstrate that a peak at 55.9 eV appears after pre-lithiation, revealing the presence of Li–O bonds in Li–VONB (Figure 4d), and in the deconvoluted V 2p spectra in Figure 4e, the presence of V^{3+} valence state is a result from charge compensation for the inserted Li. All these results confirm that lithium is successfully intercalated into the lattice of V$_6$O$_{13}$ and the designed Li–VONB is obtained. Li–VONB exhibits a similar belt-like morphology to VONB (Figure 4f), and the lattice fringe of Li$_2$V$_6$O$_{13}$ could be clearly identified in the HRTEM image in Figure 4g, with an interplanar spacing of 0.58 nm, which corresponds to the (200) plane of Li$_2$V$_6$O$_{13}$. In addition, the EDS elemental mapping results show that V and O elements distribute homogeneously over the Li–VONB sample (Figure S6, Supporting Information).

To highlight the effect of pre-intercalated Li, electrochemical performance of Li–VONB was systematically studied as compared with VONB under the same characterized conditions. **Figure 5**a shows the galvanostatic charge/discharge profile of Li–VONB at a current density of 50 mA g^{-1}. Ultra-long discharge and charge plateau at ≈1.1 and ≈1.3 V are found

**ADVANCED
SCIENCE NEWS**

www.advancedsciencenews.com

**ADVANCED
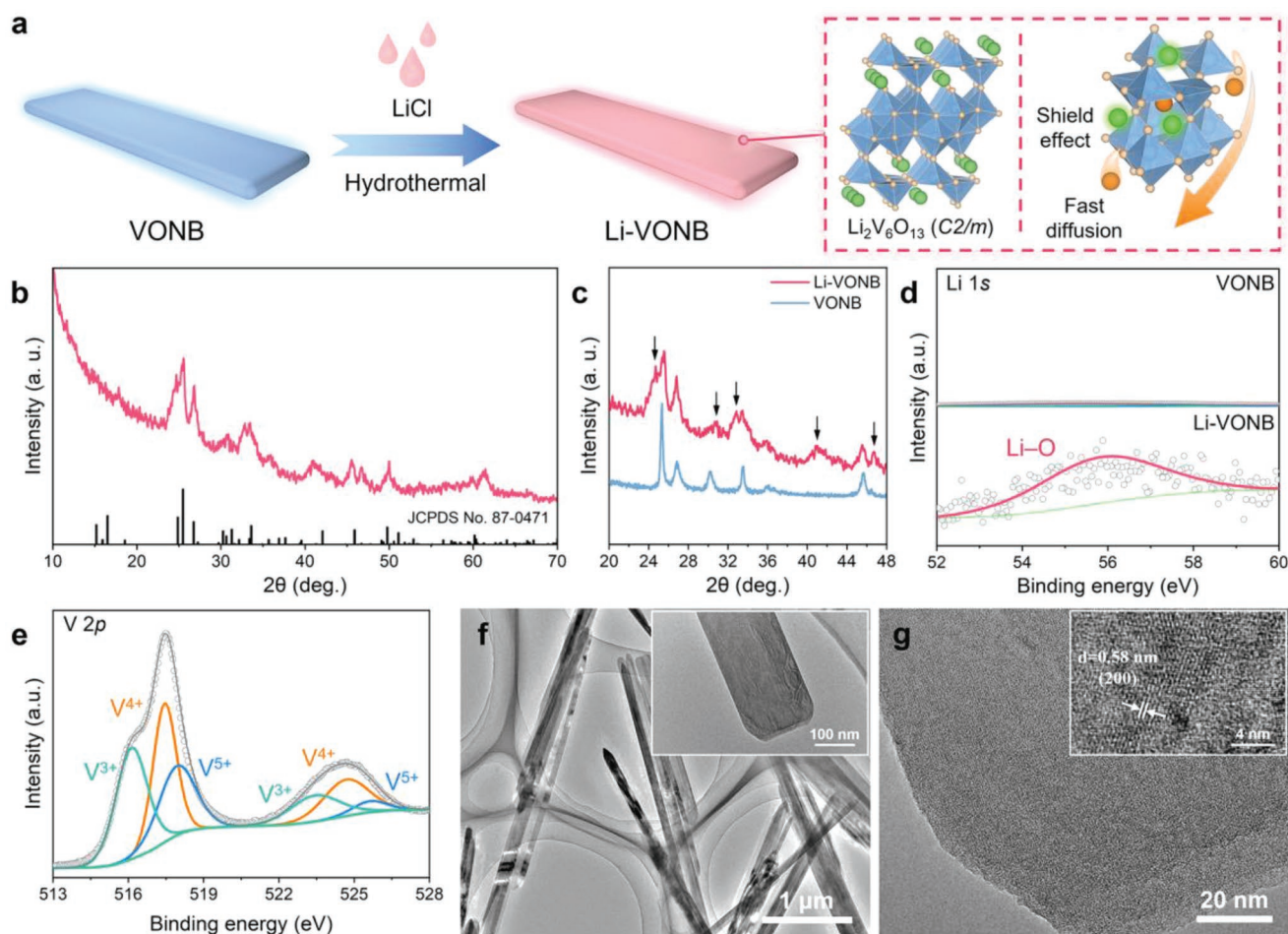ENERGY
MATERIALS**

www.advenergymat.de

Figure 4. a) Schematic illustration of preparation of Li–VONB and the Al diffusion behavior in its crystal lattice. The pre-inserted Li could effectively shield the electrostatic interactions between Al and O and promote the diffusion kinetics. b) XRD patterns of Li–VONB. c) Magnified XRD patterns of Li–VONB and VONB in the range of 20° to 48° for 2θ. The arrows inside denote the new peaks after pre-intercalation. XPS spectra of d) Li 1s and e) V 2p for Li–VONB. f) TEM and g) HRTEM images of Li–VONB.

respectively, and the curves overlap well even after 50 cycles, indicating the improved reversibility of Li–VONB. The cyclic voltammogram (CV) profiles in Figure 5b further confirm the electrochemical potential of Li–VONB with a cathodic peak at 1.06 V and an anodic peak at 1.32 V, in good agreement with the plateaus from charge/discharge profile. Compared with the CV profile of VONB, Li–VONB exhibits increased current intensity and decreased voltage hysteresis. In combination with the raised initial specific capacity of 233.28 mAh g^{-1}, it could be concluded that the electrochemical reactions in Li–VONB are promoted by the pre-intercalated Li. Furthermore, ex situ XPS analysis was conducted to check the effect of pre-intercalated Li on electrochemical mechanism. As shown in the Li 1s spectra in Figure S7, Supporting Information, the appearance of Li signal, and the comparable peak intensity and area at both fully discharged and charged states are obtained, indicating that Li ions are stable in the interstitial sites in Li–VONB during cycling. Quantitatively, the Li contents in Li–VONB during cycling were measured by the ratio of Li to V (R_{Li}) in XPS results. The ratio values for samples at different stages are similar within the uncertainty of XPS

measurements (Figure S8, Supporting Information). Besides, the Li contents in the electrolyte which were acquired by inductively coupled plasma optical emission spectroscopy (ICP-OES) measurements are listed in Table S1, Supporting Information. The fact that Li is hardly detected in the electrolyte further confirmed that Li ions are not extracted from Li–VONB host in the electrochemical process. All these results suggest that the pre-intercalated Li is not involved in the intercalation/de-intercalation reactions. In atomic scale, Li ions are all bonded with five O atoms forming a square pyramidal coordination without occupying the intercalation sites of Al. These Li ions act as "pillar" to stabilize the crystalline framework, which is evidenced by the smaller volume expansion of Li–VONB (0.6%) than that of VONB (2.1%) after Al intercalation. The robust electrode skeleton of Li–VONB is favorable to the long-term cycling stability, and the calculated E_f for Al inserting in Li–VONB is −5.53 eV, indicating that Li–VONB is suitable for Al storage thermodynamically (Figure 5c). Therefore, the electrochemical mechanism of Li–VONB is the same as that of VONB, that is, Al ions intercalate into Li–VONB in the discharging process and de-intercalate during charging.
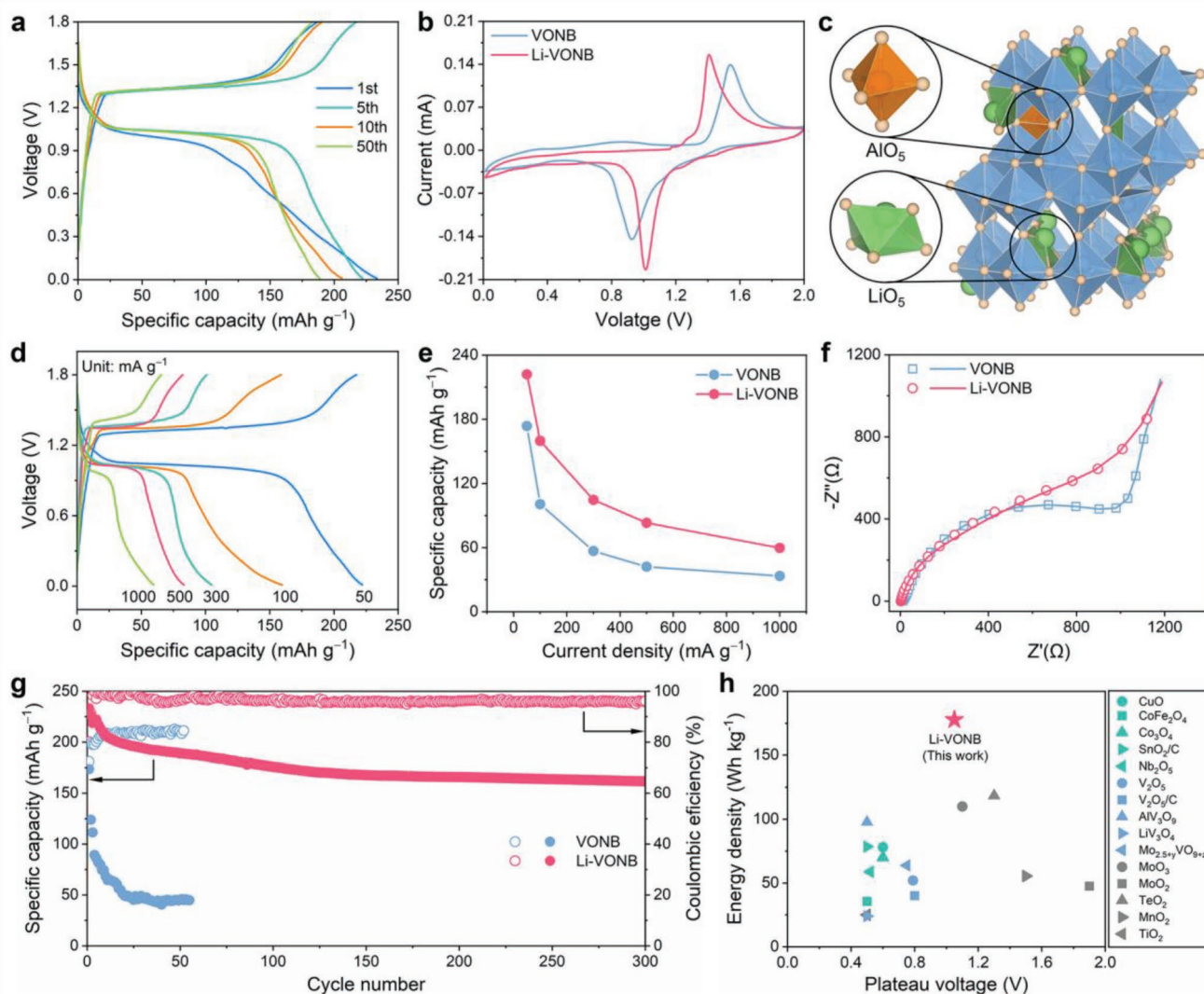
**ADVANCED
SCIENCE NEWS**
www.advancedsciencenews.com

**ADVANCED
ENERGY
MATERIALS**
www.advenergymat.de

Figure 5. a) Galvanostatic charge/discharge profiles of Li–VONB cathode under 50 mA g^{-1}. b) CV curves of Li–VONB and VONB at a scan rate of 0.5 mV s^{-1}. c) Optimized intercalation configuration of Al in Li–VONB. d) Charge/discharge profiles of Li–VONB cathode at various current densities. e) Discharge capacity of Li–VONB and VONB at current densities from 50 to 1000 mA g^{-1}. f) EIS spectra of Li–VONB and VONB. g) Cycling performance of Li–VONB and VONB at 50 mA g^{-1}. h) Comparison of energy density and plateau voltage of Li–VONB with other reported oxide cathodes in nonaqueous AIBs.

The electrochemical properties of VONB and Li–VONB at different current densities were investigated to figure out the influence of pre-inserted Li on rate performance. As shown in Figure S9, Supporting Information, large voltage hysteresis and dramatic capacity degeneration are observed for VONB at high current densities. In contrast, the charge/discharge plateaus of Li–VONB are well maintained even increasing the current density to 1000 mA g^{-1}, signifying the enhanced reaction kinetics in Li–VONB (Figure 5d). The specific capacities of Li–VONB are 221.9, 159.7, 104.6, 83.2, and 59.7 mAh g^{-1} under 50, 100, 300, 500, and 1000 mA g^{-1}, respectively, much higher than that of VONB, affirming the improved rate capability of Li–VONB (Figure 5e). In addition, galvanostatic intermittent titration technique (GITT) was employed to offer further insight into the diffusion behavior of Al^{3+} in VONB and Li–VONB. In the

GITT curves in Figure S10, Supporting Information, Li–VONB cathode exhibits a higher discharge capacity with a smaller overpotential gap than VONB, which is consistent with the CV results. Thereafter, the Fick's second law was utilized to calculate the Al^{3+} diffusion coefficients (*D*) in VONB and Li–VONB. The as-gained diffusion coefficients at different voltages are plotted in Figure S11, Supporting Information, in which the Li–VONB delivers a relatively fast ions migration rate. These results suggest that the diffusion processes and reaction rates are accelerated by pre-intercalated Li, which contributes greatly to the reversibility and kinetic properties of Li–VONB cathode. Li–VONB exhibits advantage in charge transfer as well, as identified by the depressed semicircle in electrochemical impedance spectroscopy (EIS) measurement, which is conductive to its Al^{3+} storage performance (Figure 5f). This feature was further

confirmed by the metallic characteristic of Li–VONB as indicated in PDOS plot (Figure S12, Supporting Information). The cyclic stability of Li–VONB was significantly improved after pre-lithiation as shown in Figure 5g. The reversible capacity gradually stabilizes at 50 mA g^{-1} and after 300 cycles the discharge capacity remains 161.6 mAh g^{-1} with a Coulombic efficiency of 96%. As a contrast, the specific capacity of VONB decreases to 45.4 mAh g^{-1} after only 50 cycles, and the Coulombic efficiency is 84.1%. The great enhancement in cycling performance is undoubtedly originated from the pre-intercalated Li. Besides, the electrochemical properties of the sample that is physically mixed by LiCl and VONB (denoted as LiCl/VONB) were evaluated at 50 mA g^{-1} as well. LiCl/VONB delivers similar charge/discharge curves with Li–VONB and VONB, however, its specific capacity decays to 33.8 mAh g^{-1} in only 20 cycles (Figure S13, Supporting Information), implying that Li embedded in the V$_6$O$_{13}$ lattice is the key for the improved electrochemical performance. Furthermore, the energy densities of various oxide cathodes in nonaqueous AIBs are summarized in Figure 5h and Table S2, Supporting Information.[8,12,13,22,25–35] Benefited from both elevated working voltage and high reversible capacity, the energy density of Li–VONB in this work could reach up to 177.7 Wh kg^{-1} (based on the weight of active materials), much higher than other reported oxide cathodes in AIBs.

DFT calculations were employed to investigate the microscopic effect of pre-intercalated Li for the diffusion behavior of Al in Li–VONB. In the crystal framework of both VONB and Li–VONB, Al could migrate to the adjacent equivalent sites along a and b axes. **Figure 6**a shows the migration path of Al along a axis in VONB. The strong electrostatic interaction between cationic Al and anionic O leads to a high energy barrier of 2.19 eV (Figure 6b). In the direction of b axis, the lattice deformation induced by electrostatic interaction could be observed, and Al needs to overcome an energy barrier of 1.96 eV
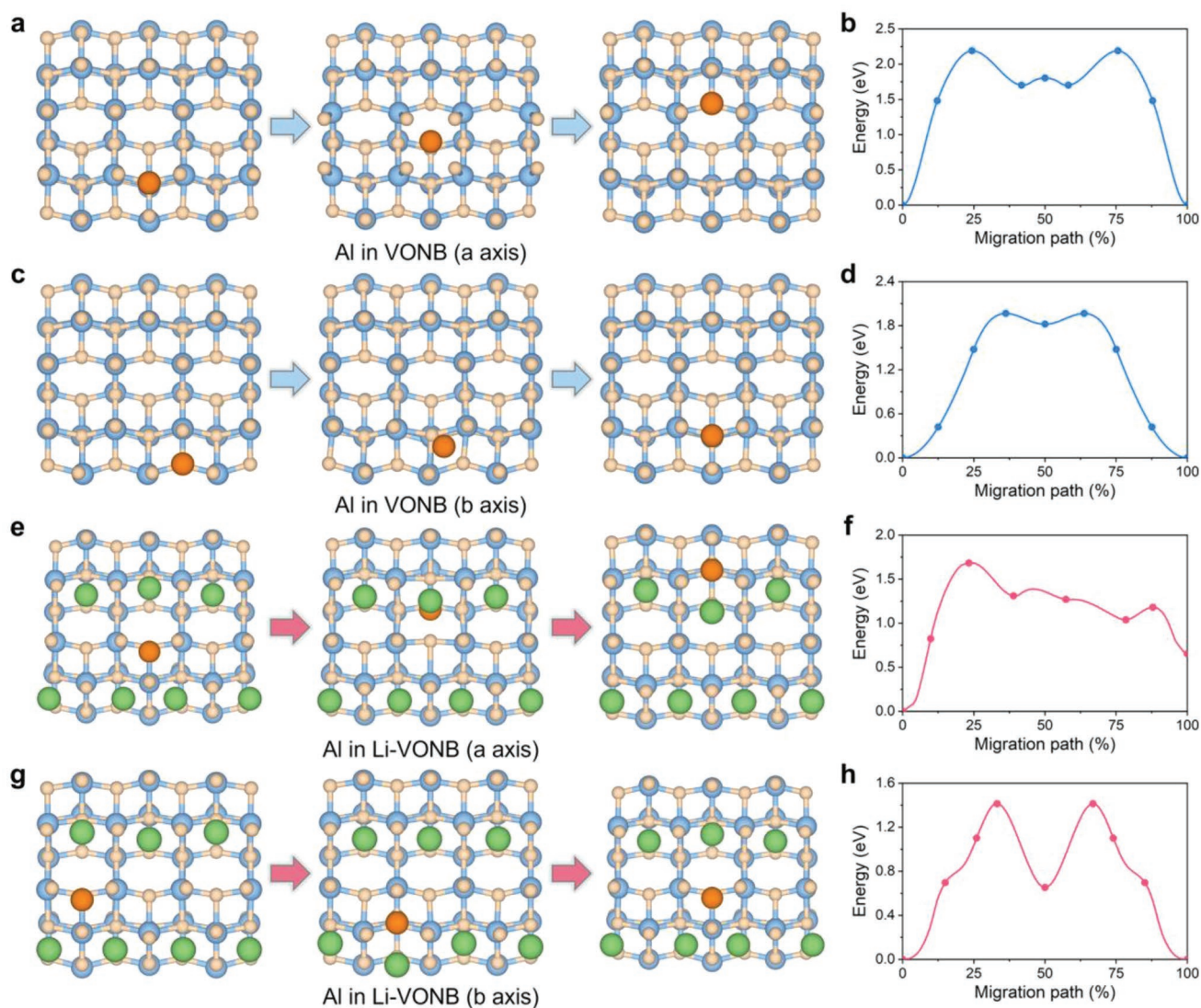

Figure 6. Al diffusion pathways and corresponding energy profiles in VONB along a axis (a,b) and along b axis (c,d). Al diffusion pathways and corresponding energy profiles in Li–VONB along a axis (e,f) and along b axis (g,h). The V, O, Li, and Al atoms are depicted in blue, yellow, green, and orange, respectively.

to hop to the neighboring sites (Figure 6c,d). In Li–VONB, a part of electrons of O are attracted by the pre-intercalated Li, reducing the electrostatic force acting on Al, which is electrostatic shielding effect of the pre-inserted Li. This phenomenon also alleviates lattice distortion, indicating that the pre-inserted Li act as "pillar" to increase the structural stability. Besides, it is interesting to find that the pre-intercalated Li relaxes away from the Al diffusion path due to the repulsion interaction between them, which deviates the migrated Al from its most stable site and makes it more active along the diffusion path. These results indicate that the pre-intercalated Li mitigate the lattice distortion, activate the charge carrier, and facilitate the migration process by its shield effect. As a result, the diffusion barriers of Al decrease to as low as 1.68 eV in a axis (Figure 6e,f) and 1.41 eV in b axis (Figure 6g,h), which contributes to the smooth intercalation/de-intercalation and accelerated diffusion kinetics of Li–VONB, and is favorable to the overall improvements in the electrochemical performance.

3. Conclusion

In summary, the predicted high-voltage V_6O_{13} cathode material was investigated by means of electrochemical characterizations, ex situ XRD and XPS measurements combined with DFT calculations, and the aluminum storage and diffusion mechanism based on Al^{3+} intercalation/de-intercalation were unraveled. Furthermore, pre-lithiation strategy was carried out to develop Li–VONB cathode for high-energy AIBs. The pre-inserted Li could promote the migration process by shielding the electrostatic interactions and act as "pillar" to stabilize the crystal framework. Benefiting from the superiority of accelerated reaction kinetics and structural stability, Li–VONB showed advantages in operating voltage ($\approx$1.1 V) and cyclic stability (a reversible capacity of 161.6 mAh g^{-1} after 300 cycles under 50 mA g^{-1}), endowing it with remarkable energy density of 177.7 Wh kg^{-1}. This work illustrates the potentiality of V_6O_{13} cathode for AIBs application, and presents an effective route toward the development of high-performance cathode materials for aluminum storage.

4. Experimental Section

Synthesis of VONB: Typically, 476.2 mg ammonium metavanadate (NH_4VO_3) and 504.2 mg oxalic acid dihydrate ($C_2H_2O_4\cdot2H_2O$) were dissolved in 40 mL deionized water. The solution was transferred into a 100 mL Teflon lined autoclave and heated at 180 °C for 8 h in a convection oven. The green powder ($NH_4V_4O_{10}$) was collected after centrifugation and vacuum drying. Subsequently, this powder was calcined in tube furnace at 450 °C for 8 h under argon with heating rate of 2 °C min^{-1}.

Synthesis of Li–VONB: VONB and lithium chloride monohydrate were fully dispersed in deionized water with mass ratio of 2:3. The solution was transferred into a 50 mL Teflon lined autoclave and kept at 180 °C for 24 h. After washing with deionized water and drying, the final Li–VONB product was obtained.

Characterization: Powder XRD patterns were measured on an X-ray diffractometer (Bruker D8 Advanced) using monochromatic Cu Kα as a radiation source. SEM images were obtained from a field emission SEM (JEOL 7500FA); TEM images were acquired on TEM (JEOL 2011 F) coupled with an EDX spectrometer. XPS spectra were achieved from an X-ray photoelectron spectrometer (PerkinElmer PHI 5000G ESGA).

Electrochemical Measurements: Electrochemical performance of VONB and Li–VONB cathode in AIBs were evaluated in Swagelok-type cells, using aluminum foil as the counter electrode, glass fiber (GF/D) as separator, and ionic liquid (the mixture of 1-ethyl-e-methylimidazolium chloride ([EMIm]Cl) and anhydrous AlCl$_3$ with the molar ratio of 1:1.3) as electrolyte. About 12 µL cm^{-2} electrolyte was added to wet the separator and cathode. The working electrodes were prepared by coating the slurry containing of the active materials, conductive carbon black, and polyvinylidene fluoride (PVDF) with the mass ratio of 7:2:1 dissolved in N-methylpyrrolidone solution on molybdenum foil, followed by drying at 80 °C under vacuum overnight. The mass loading of active materials in the electrode was ≈1.2 mg cm^{-2}. Galvanostatic charge/discharge measurements were carried out on a LAND-CT2001A battery test system. CV and EIS were conducted on VMP-3 electrochemical workstation (Bio-Logic).

Computational Methods: DFT calculations were carried out using Vienna ab initio simulation package (VASP).[36,37] Core-valence electron interaction was described by the projector-augmented wave (PAW) method,[38,39] and electron exchange-correlation was processed by generalized gradient approximation of Perdew–Burke–Ernzerhof functional.[40] The van der Waals correction DFT-D3 proposed by Grimme was employed to include the dispersion interaction.[41] A plane wave energy cutoff of 520 eV and Gamma centered k-point meshes with same density were applied to surface calculations. The Gaussian smearing method was used with a width of 0.05 eV, and spin polarization was considered in all calculations. The structures were relaxed until the forces and total energy on all atoms were converged to less than 0.05 eV Å^{-1} and 1×10^{-5} eV. The diffusions of Al in Li–VONB and VONB are simulated using the climbing-image nudged elastic band (CI-NEB) method.[42,43] Six images were applied to these calculations. The formation energies (E_f) of Al intercalation into various vanadium oxides are calculated as

$$E_f = E_{Total} - E_{Al} - E_{VO} \qquad (1)$$

where E_{Total} and E_{VO} are the energies of the complex with Al intercalated and pristine vanadium oxides, respectively. E_{Al} is the energy per atom for the bulk Al. A negative value of E_f indicates that Al insertion is thermodynamically favorable. The average intercalation voltage is

$$V = -E_f/ez \qquad (2)$$

where e is the elementary charge and z is the number of electron transferred per inserted atom ($z = 3$ for Al).

Supporting Information

Supporting Information is available from the Wiley Online Library or from the author.

Conflict of Interest

The authors declare no conflict of interest.

Data Availability Statement

The data that support the findings of this study are available in the supplementary material of this article.

[1] Y. Zhang, S. Liu, Y. Ji, J. Ma, H. Yu, *Adv. Mater.* **2018**, *30*, 1706310.

[2] H. Yang, H. Li, J. Li, Z. Sun, K. He, H. M. Cheng, F. Li, *Angew. Chem., Int. Ed.* **2019**, *58*, 11978.

[3] Z. A. Zafar, S. Imtiaz, R. Razaq, S. Ji, T. Huang, Z. Zhang, Y. Huang, J. A. Anderson, *J. Mater. Chem. A* **2017**, *5*, 5646.

[4] M. C. Lin, M. Gong, B. Lu, Y. Wu, D. Y. Wang, M. Guan, M. Angell, C. Chen, J. Yang, B. J. Hwang, H. Dai, *Nature* **2015**, *520*, 324.

[5] D. J. Kim, D.-J. Yoo, M. T. Otley, A. Prokofjevs, C. Pezzato, M. Owczarek, S. J. Lee, J. W. Choi, J. F. Stoddart, *Nat. Energy* **2018**, *4*, 51.

[6] Z. Lin, M. Mao, C. Yang, Y. Tong, Q. Li, J. Yue, G. Yang, Q. Zhang, L. Hong, X. Yu, L. Gu, Y. S. Hu, H. Li, X. Huang, L. Suo, L. Chen, *Sci. Adv.* **2021**, *7*, eabg6314.

[7] T. Koketsu, J. Ma, B. J. Morgan, M. Body, C. Legein, W. Dachraoui, M. Giannini, A. Demortiere, M. Salanne, F. Dardoize, H. Groult, O. J. Borkiewicz, K. W. Chapman, P. Strasser, D. Dambournet, *Nat. Mater.* **2017**, *16*, 1142.

[8] Z. Li, J. Li, F. Kang, *Electrochim. Acta* **2019**, *298*, 288.

[9] Y. Hu, D. Ye, B. Luo, H. Hu, X. Zhu, S. Wang, L. Li, S. Peng, L. Wang, *Adv. Mater.* **2018**, *30*, 1703824.

[10] C. Liu, Z. G. Neale, G. Cao, *Mater. Today* **2016**, *19*, 109.

[11] J. L. Shi, D. D. Xiao, M. Ge, X. Yu, Y. Chu, X. Huang, X. D. Zhang, Y. X. Yin, X. Q. Yang, Y. G. Guo, L. Gu, L. J. Wan, *Adv. Mater.* **2018**, *30*, 1705575.

[12] A. M. Diem, J. Bill, Z. Burghard, *ACS Appl. Energy Mater.* **2020**, *3*, 4033.

[13] W. Kaveevivitchai, A. Huq, S. Wang, M. J. Park, A. Manthiram, *Small* **2017**, *13*, 1701296.

[14] F. Wu, H. Yang, Y. Bai, C. Wu, *Adv. Mater.* **2019**, *31*, 1806510.

[15] Y. Liu, J. Xu, J. Li, Z. Yang, C. Huang, H. Yu, L. Zhang, J. Shu, *Coord. Chem. Rev.* **2022**, *460*, 214477.

[16] H. D. Yoo, Y. Liang, H. Dong, J. Lin, H. Wang, Y. Liu, L. Ma, T. Wu, Y. Li, Q. Ru, Y. Jing, Q. An, W. Zhou, J. Guo, J. Lu, S. T. Pantelides, X. Qian, Y. Yao, *Nat. Commun.* **2017**, *8*, 339.

[17] Y. Yang, Y. Tang, G. Fang, L. Shan, J. Guo, W. Zhang, C. Wang, L. Wang, J. Zhou, S. Liang, *Energy Environ. Sci.* **2018**, *11*, 3157.

[18] W. Li, K. Wang, S. Cheng, K. Jiang, *Adv. Energy Mater.* **2019**, *9*, 1900993.

[19] H. Tang, F. Xiong, Y. Jiang, C. Pei, S. Tan, W. Yang, M. Li, Q. An, L. Mai, *Nano Energy* **2019**, *58*, 347.

[20] V. V. Kulish, D. Koch, S. Manzhos, *Phys. Chem. Chem. Phys.* **2017**, *19*, 6076.

[21] V. V. Kulish, S. Manzhos, *RSC Adv.* **2017**, *7*, 18643.

[22] J. Jiang, H. Li, J. Huang, K. Li, J. Zeng, Y. Yang, J. Li, Y. Wang, J. Wang, J. Zhao, *ACS Appl. Mater. Interfaces* **2017**, *9*, 28486.

[23] H. Wang, Y. Bai, S. Chen, X. Luo, C. Wu, F. Wu, J. Lu, K. Amine, *ACS Appl. Mater. Interfaces* **2015**, *7*, 80.

[24] P. He, J. Liu, X. Zhao, Z. Ding, P. Gao, L.-Z. Fan, *J. Mater. Chem. A* **2020**, *8*, 10370.

[25] M. Chiku, H. Takeda, S. Matsumura, E. Higuchi, H. Inoue, *ACS Appl. Mater. Interfaces* **2015**, *7*, 24385.

[26] J. Tu, M. Wang, Y. Luo, S. Jiao, *ACS Sustainable Chem. Eng.* **2020**, *8*, 2416.

[27] P. Almodóvar, D. A. Giraldo, J. Chancón, I. Álvarez-Serrano, M. L. López, *ChemElectroChem* **2020**, *7*, 2102.

[28] Z. Li, W. Lv, G. Wu, X. Li, X. Wang, W. Zhang, *Chem. Eng. J.* **2022**, *430*, 133135.

[29] N. Zhu, F. Wu, Z. Wang, L. Ling, H. Yang, Y. Gao, S. Guo, L. Suo, H. Li, H. Xu, Y. Bai, C. Wu, *J. Energy Chem.* **2020**, *51*, 72.

[30] X. Zhang, G. Zhang, S. Wang, S. Li, S. Jiao, *J. Mater. Chem. A* **2018**, *6*, 3084.

[31] F. Nacimiento, M. Cabello, R. Alcántara, C. Pérez-Vicente, P. Lavela, J. L. Tirado, *J. Electrochem. Soc.* **2018**, *165*, A2994.

[32] K. Zhang, T. H. Lee, J. H. Cha, H. W. Jang, J. W. Choi, M. Mahmoudi, M. Shokouhimehr, *Sci. Rep.* **2019**, *9*, 13739.

[33] H. Lu, Y. Wan, T. Wang, R. Jin, P. Ding, R. Wang, Y. Wang, C. Teng, L. Li, X. Wang, D. Zhou, G. Xue, *J. Mater. Chem. A* **2019**, *7*, 7213.

[34] L. Wang, H. Lin, W. Kong, Y. Hu, R. Chen, P. Zhao, M. Shokouhimehr, X. L. Zhang, Z. Tie, Z. Jin, *Nanoscale* **2020**, *12*, 12531.

[35] J. Wei, W. Chen, D. Chen, K. Yang, *J. Electrochem. Soc.* **2017**, *164*, A2304.

[36] G. Kresse, J. Furthmüller, *Comput. Mater. Sci.* **1996**, *6*, 15.

[37] G. Kresse, J. Hafner, *Phys. Rev. B* **1994**, *49*, 14251.

[38] G. Kresse, D. Joubert, *Phys. Rev. B* **1999**, *59*, 1758.

[39] P. E. Blochl, *Phys. Rev. B* **1994**, *50*, 17953.

[40] P. P. John, B. Kieron, E. Matthias, *Phys. Rev. Lett.* **1996**, *77*, 3865.

[41] S. Grimme, J. Antony, S. Ehrlich, H. Krieg, *J. Chem. Phys.* **2010**, *132*, 154104.

[42] J. Paier, R. Hirschl, M. Marsman, G. Kresse, *J. Chem. Phys.* **2005**, *122*, 234102.

[43] A. Heyden, A. T. Bell, F. J. Keil, *J. Chem. Phys.* **2005**, *123*, 224101.